ACS APPLIED MATERIALS & INTERFACES

Research Article

www.acsami.org

Carbon-Deposited TiO_2 3D Inverse Opal Photocatalysts: Visible-Light Photocatalytic Activity and Enhanced Activity in a Viscous Solution

Sunbok Lee,[†,‡] Youngshin Lee,[†,‡] Dong Ha Kim,[§] and Jun Hyuk Moon*[,†]

[†]Department of Chemical and Biomolecular Engineering, Sogang University, Seoul 121-742, Republic of Korea

[§]Department of Chemistry and Nano Science, Global Top 5 Research Program, Ewha Womans University, 52 Ewhayeodae-gil, Seodaemun-gu, Seoul, 120-750, Republic of Korea

Supporting Information

ABSTRACT: We for the first time demonstrated carbon-deposited TiO_2 inverse opal (C-TiO_2 IO) structures as highly efficient visible photocatalysts. The carbon deposition proceeded via high-temperature pyrolysis of phloroglucinol/formaldehyde resol, which had been coated onto the TiO_2 IO structures. Carbon deposition formed a carbon layer and doped the TiO_2 interface, which synergistically enhanced visible-light absorption. We directly measured the visible-light photocatalytic activity by constructing solar cells comprising the C-TiO_2 IO electrode. Photocatalytic degradation of organic dyes in a solution was also evaluated. Photocatalytic dye degradation under visible light was only observed in the presence of the C-TiO_2 IO sample and was increased with the content of carbon deposition. The IO structures could be readily decorated with TiO_2 nanoparticles to increase the surface area and enhance the photocatalytic activity. Notably, the photocatalytic reaction was found to proceed in a viscous polymeric solution. A comparison of the mesoporous TiO_2 structure and the IO TiO_2 structure revealed that the latter performed better as the solution viscosity increased. This result was attributed to facile diffusion into the fully connected and low-tortuosity macropore network of the IO structure.

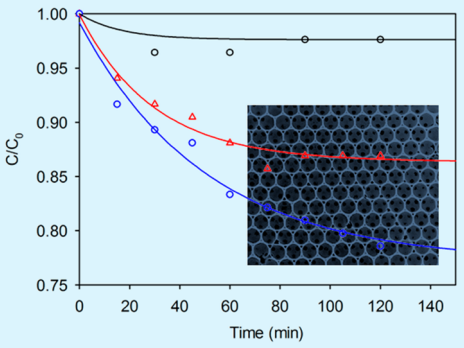

KEYWORDS: *inverse opals, carbon deposition, photocatalysts, visible-light activity, viscous solution*

INTRODUCTION

Photocatalysts have been explored for their utility in environmental applications, such as pollutant dissociation,[1,2] photon-to-electric energy conversion devices,[3,4] or water-splitting applications.[5,6] TiO_2 has been widely applied as a photocatalyst because it is chemically stable, abundant in nature, and low in cost.[7] Because TiO_2 has a wide band gap (3.0 eV for the anatase structure and 3.2 eV for the rutile structure),[8] the absorption of visible light and longer wavelengths is limited, and thus the efficiencies of photocatalytic reactions under sunlight are low. In an effort to extend the TiO_2 photoresponse spectrum to the visible region, studies have attempted to introduce transition metals (e.g., Fe or S) or nonmetals (e.g., N, C, or B) as dopants[9−12] or dyes, semiconductor nanocrystals, or carbonaceous materials as sensitizers.[2,13−17] The introduction of doping agents into TiO_2 could reduce the TiO_2 electronic band gap or create localized electronic states in the band gap that could improve the direct absorption of visible light. Sensitizers, on the other hand, absorb visible light directly and release electrons to TiO_2 in an oxidizing reaction. The use of carbon materials has been attractive for several reasons.[17−23] Carbon absorbs over a wide range of visible light to provide efficient sensitizer functionality.[17] Carbon can be obtained in a variety of functional allotropes, including carbon nanotubes and graphene. Recently, graphene/TiO_2 composites were shown to display high photocatalytic activities because graphene provides a high surface area and good electrical conductivity, thereby facilitating the transfer of photogenerated electrons to a solution-based pollutant and inducing degradation of the pollutant.[2,24] Moreover, organic pollutants adsorb readily to carbon, which is a prerequisite for pollutant decomposition.

Nanostructures in photocatalysts have been identified as another important factor for the photocatalytic activity.[25] Photogenerated electrons must be able to avoid electron−hole recombination reactions long enough to induce a catalytic reaction at the surface. The nanostructure morphology can elongate electron−hole separation by the facile transport of electrons. Efficient photocatalytic degradation of pollutants in a solution requires that the pollutant molecules diffuse into the pores of the catalyst, which are preferable in a highly porous and well-connected pore structure. In this regard, there have been many reports on 1D nanostructures, such as nanotubes or nanowires.[26−29] 3D porous structures, such as ordered mesoporous structures or inverse opals (IOs), have revealed efficient photocatalytic activity.[24,30−32]

Received: September 5, 2013
Accepted: November 15, 2013
Published: November 22, 2013

In this Article, we, for the first time, report the preparation of carbon-deposited TiO_2 (C-TiO_2) IO structures for use as highly efficient photocatalysts under visible-light illumination. Previous studies of IO structures have sought to enhance the photocatalytic properties either by tuning the photonic band gap[33,34] or by improving the visible spectrum absorption by using WO_3[35] and Bi_2WO_6[36] IOs or a graphene-incorporated TiO_2 IO.[24] Here, carbon was both deposited, forming a carbon layer, and doped into the TiO_2 structure at the interface, which synergistically enhanced the visible-light photocatalytic activity. We also demonstrated a direct measurement of the photocurrent by constructing a solar cell using C-TiO_2 IO electrodes. Moreover, the photocatalytic reaction was measured in a viscous polymeric solution. Viscous solutions are more relevant to practical environments for photocatalyst applications than are aqueous solutions. The fully connected macropore network of the C-TiO_2 IO structure yielded enhanced photocatalytic performances in a viscous solution.

EXPERIMENTAL SECTION

Fabrication of TiO_2 IOs. A monodisperse polystyrene colloid solution (diameter 740 nm) was synthesized via dispersion polymerization of a mixture of styrene monomers (10 w/v %), poly(vinylpyrrolidone) stabilizers (20 w/v %), and 2,2-azobis(2-methylbutyronitrile) (1 wt % of monomer) as the photoinitiator. The polystyrene (PS) colloids were deposited on a substrate, and the solvent was evaporated to obtain a colloidal crystal template film. The TiO_2 nanocolloid (average size 15 nm, dispersed in water, Nanoamor Inc.) was infiltrated into the PS colloidal crystals by spin coating. The TiO_2/nanoparticle (NP) composite and the PS colloidal crystals were calcined to remove the template, resulting in a TiO_2 IO structure.

Carbon Deposition. A resol (carbon precursor) was prepared from phloroglucinol [$C_6H_3(OH)_3$] and formaldehyde in a base-catalyzed process. Note that the phloroglucinol/formaldehyde (PF) resol was prepared instead of the more widely used phenol/formaldehyde because the phloroglucinol polymerization reaction proceeded much faster (within a few hours) than the phenol polymerization reaction (within a few days). In a typical process, 0.01 mol of phloroglucinol was dissolved in an ethanol/water mixture solution (50:50). The solution was mixed with a small amount of a 20 wt % sodium hydroxide aqueous solution for 2 h. Then, 0.17 mol of 37 wt % formaldehyde were added to the solution dropwise to produce the PF resol. The carbon was deposited by spin-coating the PF resol (at 3000 rpm) onto the TiO_2 IOs and subsequently applying heat treatment at 850 °C for 3 h under a N_2 atmosphere to pyrolyze the PF resol into carbon. The amount of carbon deposited was controlled by tuning the concentration of the PF resol in ethanol. The concentrations of the PF resol solutions used in this experiment were 1 or 5 wt %.

Photocurrent and Photocatalytic Activity Measurements. The artificial visible-light source was obtained from a solar simulator (1000 W xenon lamp with AM 1.5G filter) and optical filters; the light intensity of the solar simulator was adjusted to 100 mW cm^{-2} using a silicon reference cell and then directed through short- and long-pass filters (Thorlabs Inc.) to obtain light with a wavelength range of 495–700 nm. The photocurrent was measured by constructing a device similar to the dye-sensitized solar cell.[3] The cell was assembled using a C-TiO_2 IO electrode, a platinum-coated counter electrode, and an iodine/iodide electrolyte. The photocurrent density was measured using a source meter (Keithley Instruments) under visible-light illumination. The photocatalytic activity was evaluated by monitoring the degradation of methylene blue (MB) under visible-light illumination. The C-TiO_2 IO samples (a typical area of 2.0 cm × 2.0 cm) were placed in a 0.5 μM MB solution. The degradation of MB was monitored by measuring the optical absorbance of the MB solution. The maximum absorbance of MB occurred at 650–665 nm, and this peak intensity could be converted to the MB concentration using a Beer–Lambert calibration curve. For measurement of the photocatalytic activity in a viscous solution, the solution was prepared by dissolving 0.5 or 1 wt % polyacrylamide (PAA; M_w = 5000000, Aldrich) in a 0.5 μM MB solution. A mesoporous TiO_2 film was fabricated by coating commercial TiO_2 colloidal paste (Dyesol, 18NR-T).[37] The film was heat-treated at 500 °C for 2 h in air.

Characterization Studies. The surface morphologies were characterized by scanning electron microscopy (SEM; Hitachi S4700). The TiO_2 phase was confirmed by measuring the X-ray diffraction (XRD; Rigaku) patterns using Cu Kα radiation. The absorbance and diffuse-reflectance spectra of the samples were characterized using UV–vis spectrophotometry (Shimadzu UV-2550). The carbon atom content was determined by collecting energy-dispersive spectroscopy (EDS) measurements in conjunction with the SEM measurements. The properties of the carbon layer were analyzed by X-ray photoelectron spectroscopy (XPS) and Raman spectrometry at an emission wavelength of 514.5 nm.

RESULTS AND DISCUSSION

The TiO_2 IO structures shown in Figure 1a were prepared by a PS colloidal crystal template (see Figure S1 in the Supporting Information). Here, the PS colloid was prepared in ethanol via dispersion polymerization to prepare a uniform adhesive coating of the PS colloidal crystal film. The rapid evaporation of ethanol tended to release the stress that built up in the PS colloidal film and induced film delamination. The PS particle size was around 700 nm diameter, and the macropore size in the TiO_2 structure was around 500 nm. The macropores shrank by 28% of the original particle size because of thermal effects during template removal. The inset image in Figure 1a shows a cross-sectional image of a TiO_2 IO film, revealing a film thickness of around 30 μm. The quantity of carbon deposited on TiO_2 IO was controlled by varying the concentration of the PF resol in the coating solution. PF resol ethanol solutions having concentrations of 1.0 or 5.0 wt % were applied, and conversion of the precursor into carbon was achieved by heating at 850 °C under a N_2 atmosphere. For comparison, bare TiO_2 IO, which had been heat-treated under the same conditions, was obtained and is shown in Figure 1b. Parts c and d of Figure 1 show surface SEM images of C-TiO_2 IO prepared from the 1.0 and 5.0 wt % PF resol solutions, respectively. The

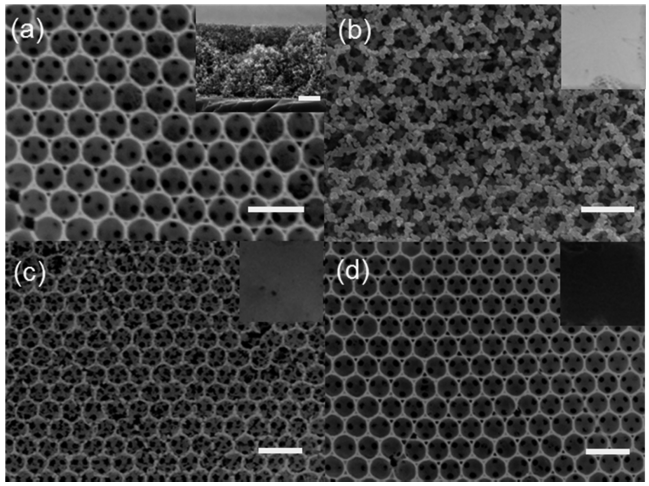

Figure 1. SEM images of (a) pristine TiO_2 IO (cross-sectional images are shown in the insets; scale bar 10 μm), (b) bare TiO_2 IO (prepared at 850 °C), (c) low-C-TiO_2 IO, and (d) high-C-TiO_2 IO. The inset images show color digital images of the corresponding samples. The scale bars are 1 μm.

carbon content, measured by EDS, revealed that the TiO_2 structures coated with 1.0 or 5.0 wt % PF resol solutions deposited 50 or 75 atom % carbon on the TiO_2 surface, and the resulting TiO_2 IO structures were abbreviated as low-C-TiO_2 IO and high-C-TiO_2 IO, respectively.

The TiO_2 IO structure prepared at 500 °C (pristine TiO_2; Figure 1a) was compared with the TiO_2 IO structure prepared by heat treatment at 850 °C (bare TiO_2; Figure 1b). The latter structure included larger primary TiO_2 particles (50−100 nm diameter) due to transformation of the anatase phase to the rutile phase.[38] However, parts c and d of Figure 1 show that, as the amount of carbon deposited increased, the size of the primary TiO_2 particles in the IO structure decreased. It is noted that high-C-TiO_2 IO displayed morphology similar to that of bare TiO_2 IO prepared at 500 °C (Figure 1a). The crystalline structures of the TiO_2 IO samples prepared with different carbon contents were characterized based on the XRD measurements, as shown in Figure 2a. The TiO_2 IO sample

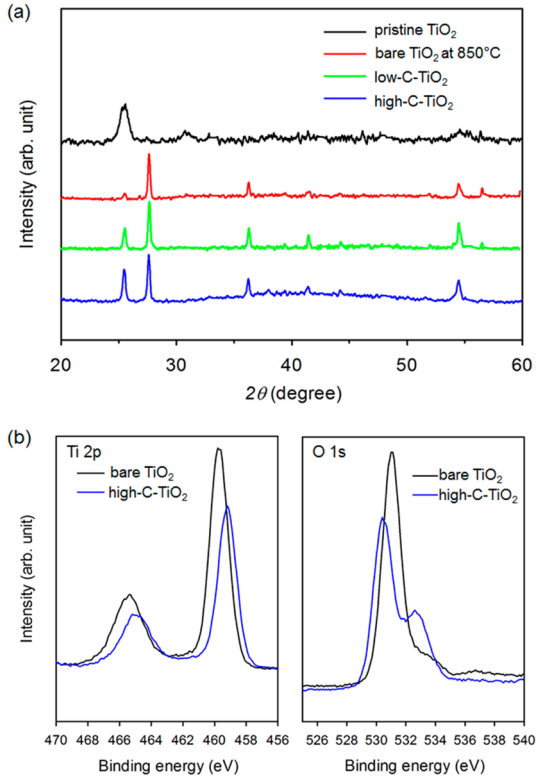

Figure 2. (a) XRD patterns of the pristine TiO_2 IO (prepared at 500 °C), bare TiO_2 IO (prepared at 850 °C), low-C-TiO_2 IO, and high-C-TiO_2 IO films. (b) XPS spectra of the bare TiO_2 IO and high-C-TiO_2 IO films.

that had been heat-treated at 500 °C displayed an anatase (101) peak at 25.4°, whereas the TiO_2 IO sample treated at 850 °C displayed an additional strong diffraction peak at 27.8°, indicating the presence of the rutile (110) phase. As the deposited carbon content increased, the ratio of the anatase (101) (25.4°) to rutile (110) peaks increased, indicating an incomplete transition into the rutile phase, as observed in the SEM images. This result is similar to the previous observation showing that when the anatase TiO_2 particle surface was impregnated by other oxide materials, phase transformation was significantly retarded because of the avoidance of direct contact between anatase primary particles.[38] The weight fractions of the rutile and anatase TiO_2 phases in these samples were quantified based on the respective peak intensities. The rutile weight fraction W_R in a sample was evaluated using the following equation:

$$W_R = 1/[1 + 0.8(I_A/I_R)]$$

where W_R, I_A, and I_R indicate the fraction of the rutile phase, the XRD peak intensity of the anatase (101) phase, and the peak intensity of the rutile (110) phase.[38] The extent of conversion from the anatase to rutile phase in low-C-TiO_2 IO or high-C-TiO_2 IO was only 50% or 10% of the extent of conversion in bare TiO_2 IO.

The deposited carbon was characterized by Raman spectroscopy, as shown in Figure S2 in the Supporting Information. Two broad bands were observed at 1360 and 1590 cm^{-1} and were attributed to the D and G bands of carbon, respectively. The D band corresponds to the A_{1g} mode and is characteristic of in-plane disorder or defects, whereas the G band corresponds to the in-plane E_{2g} vibrational mode of graphite sheets. The intensity ratio of the D to G band (I_D/I_G) indicates the degree of defects that may be present in graphitic carbon. The I_D/I_G values of the low-C-TiO_2 and high-C-TiO_2 samples were 1.02 and 1.00, respectively. Thus, the carbon in these samples showed similar amorphous carbon characteristics. Moreover, the interface between TiO_2 and carbon was investigated in detail using XPS measurements. Figure 2b shows a high-resolution Ti 2p XPS spectrum. Two peaks at 460 and 466 eV correspond to Ti^{4+} atoms. Note that the peaks were shifted toward lower energies by 1 eV relative to the TiO_2 peaks. Because the double peaks corresponding to the rutile and anatase phases occurred near the sample binding energies, this shift may be related to carbon-doping effects.[39] The O 1s spectrum in Figure 2b shows that the TiO_2 sample displayed a single peak corresponding to the oxygen groups in the lattice, whereas the corresponding C-TiO_2 IO sample peak was shifted. An additional main peak observed at 533 eV indicated the presence of carbonate oxygen atoms (C−O). The peak shift may be indicative of carbon doping.[21] Previously, carbon deposition has been achieved via high-temperature pyrolysis of a carbon precursor, which resulted in carbonate doping of the structure.[12,20] Briefly, the Raman and XPS results indicated that some of the deposited carbon had penetrated the TiO_2 lattice to act as a dopant.

The absorption properties of the low- and high-C-TiO_2 IO structures were characterized, as shown in Figure 3. The Kubelka−Munk transformed plot of the absorption spectra is also shown in Figure S3 in the Supporting Information. The absorption edge of the bare TiO_2 IO film extended to around 390 nm, consistent with the optical band gap of the rutile phase, 3.1 eV. The absorption edge of the low-C-TiO_2 IO film was shifted to 480 nm. The substitution of carbon atoms with oxygen atoms can produce a series of localized occupied states in the band gap that enable the absorption of visible light by carbon-doped TiO_2.[21,40,41] Moreover, the high absorption intensity in the visible region was attributed to the absorption properties of the carbon overlayer on the TiO_2 surface.[17,39] The absorption edge in the high-C-TiO_2 film was difficult to identify because of the strong absorption spectrum of the deposited carbon.

Here, the photocatalytic activities of the C-TiO_2 IO structures were evaluated using direct and indirect methods. First, the photocurrent generated by a C-TiO_2 IO sample under light illumination was measured to provide a direct indicator of

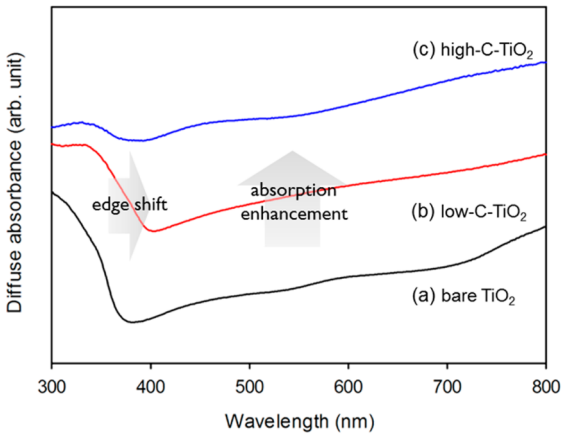

Figure 3. UV−vis diffuse-reflectance absorption spectra of the bare TiO_2 IO, low-C-TiO_2 IO, and high-C-TiO_2 IO samples.

the photocatalytic activity. Briefly, a C-TiO_2 IO film was used as a photoanode in a dye-sensitized solar cell (see the inset image of Figure 4a). The cell was assembled using a C-TiO_2 IO electrode, a platinum-coated counter electrode, and an iodine/iodide electrolyte. As shown in Figure 4a, the C-TiO_2 IO

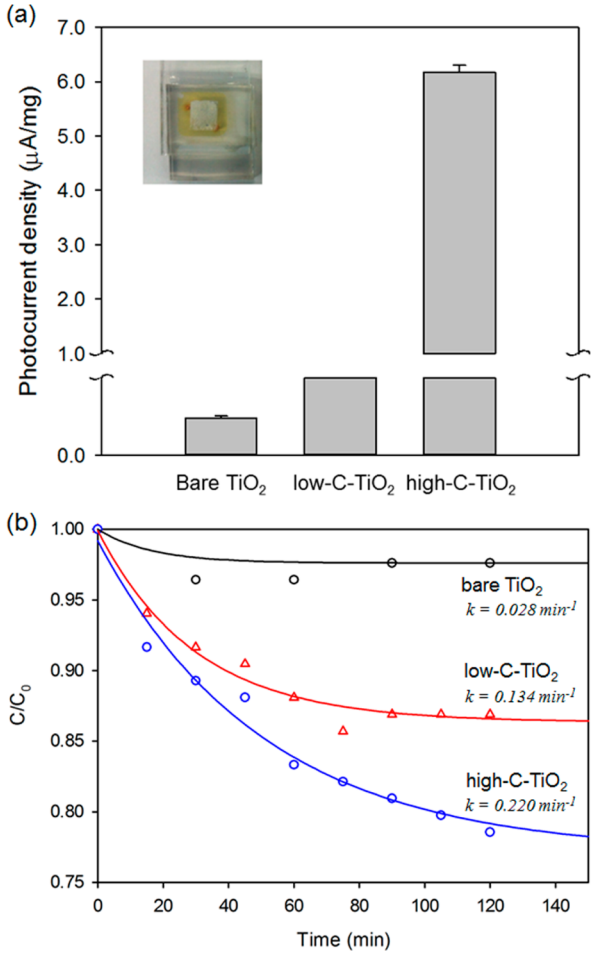

Figure 4. (a) Photocurrent densities of solar cells prepared with a bare TiO_2 IO electrode or a C-TiO_2 IO electrode under filtered visible-light illumination. (b) MB decomposition of the bare TiO_2 IO, low-C-TiO_2 IO, and high-C-TiO_2 IO films under filtered visible-light illumination.

electrode cell showed a much higher photocurrent density compared to the bare TiO_2 IO electrode cell. This result clearly confirmed that electrons were generated as a result of visible-light absorption and collected through the TiO_2 layer. The low-C-TiO_2 IO sample displayed an absorption edge at 490 nm as a result of carbon doping. Because the illumination spectrum was selected to be above this edge, the measured photocurrent of low-C-TiO_2 IO must have resulted from the sensitized absorption of deposited carbon. In the case of the high-C-TiO_2 IO sample, the photocurrent density was 40 times greater than the corresponding value of the low-C-TiO_2 IO sample. The absorption edge of the high-C-TiO_2 IO structure may be within the illumination wavelength, as shown in Figure 3. The average absorption intensity in the high C-TiO_2 IO sample over the range 495−700 nm was twice the value of the low C-TiO_2 IO sample. Thus, this high enhancement in the photocurrent suggests a synergy between the carbon-doping and carbon-sensitization effects.

The indirect measurements of the photocatalytic responses were evaluated by degrading MB dye in the presence of photocatalyst samples under visible-light illumination, as shown in Figure 4b. In general, photocatalysts absorb photons and generate electrons, which then react with H_2O to create radical oxygen species that decompose any MB molecules adsorbed onto the photocatalyst surface.[8] The MB degradation product was leucomethylene blue, which is colorless. Here, the use of a 495−700 nm illumination spectrum minimized MB degradation by UV light or thermal effects because of absorption in the IR region. The degradation was estimated from the relative decrease in the absorption peak of MB as a function of the irradiation time. Figure 4b shows the normalized concentration of the MB solution (C/C_0) during photodegradation in the presence of the various C-TiO_2 samples. The degradation of MB in the presence of bare TiO_2 IO was measured for comparison purposes. The TiO_2 IO sample clearly displayed almost no photocatalytic behaviors, whereas C-TiO_2 IO apparently induced MB degradation under visible-light illumination. The carbon-deposited samples induced more decomposition of MB molecules in solution compared to the bare TiO_2 IO sample. In order to obtain the rate constant, the decomposition curve was fit by using a pseudo-first-order reaction rate equation, y = constant + y_0 exp$(-kt)$, where y is the C/C_0, k is the reaction rate constant, and t is the time. The initial rate constants for bare TiO_2 IO, low-C-TiO_2 IO films, and high-C-TiO_2 IO were obtained to be 0.028, 0.134, and 0.220 min^{-1}, respectively. The degradation rate increased as the amount of deposited carbon increased. The higher degradation rate in the presence of the high-C-TiO_2 IO films, compared with the low-C-TiO_2 films, was attributed to a greater absorption of visible light, as shown in Figure 3. Meanwhile, the higher degradation rate (1.64-fold enhancement) of the high-C-TIO_2 IO sample was less pronounced than the measured enhancement in the photocurrent. This is possibly because, in the photocatalytic degradation reaction, the additional step of MB adsorption onto the C-TiO_2 IO surface is involved. Then, the degradation throughput is proportional to the surface area. The high-C-TiO_2 IO structure possessed a smoother surface than the low-C-TIO_2 IO structure because the presence of carbon had disrupted the anatase-to-rutile TiO_2 transition, as shown in Figure 1. The smooth surface limited the amount of MB adsorbed, which, in turn, reduced the photocatalytic degradation throughput and thereby compromised the efficient photocurrent generation.

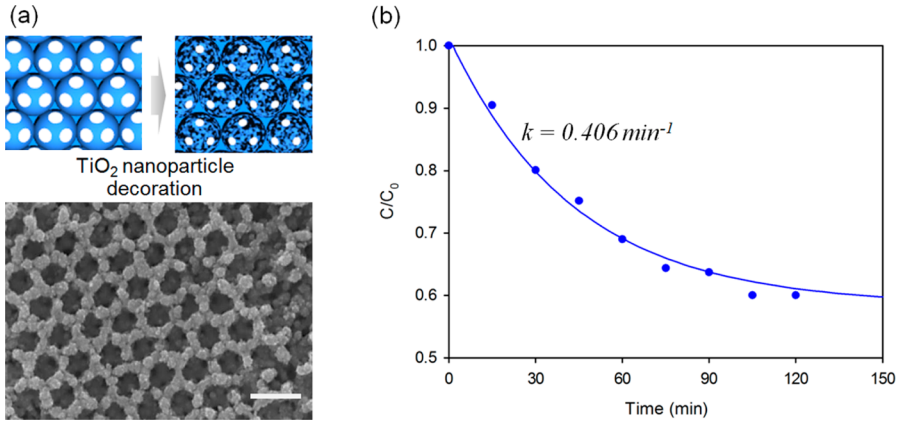

Figure 5. (a) Scheme of TiO_2 NP decoration on TiO_2 IO. SEM image of the carbon-deposited NP-TiO_2 IO structure. (b) MB decomposition in the presence of the carbon-deposited NP-TiO_2 IO film under filtered visible-light illumination. The scale bar is 1 μm.

Meanwhile, the low surface area of the high-C-TiO_2 sample could be ameliorated by increasing the surface area of the TiO_2 IO structure before carbon deposition. Here, the TiO_2 IO structure was decorated with TiO_2 NPs, and carbon was subsequently deposited as described in Figure 5a. Briefly, the TiO_2 NP decoration step was carried out via chemical bath deposition in a $TiCl_4$ precursor bath; a 0.3 M $TiCl_4$ aqueous solution bath was prepared, and deposition was achieved at 70 °C for 60−90 min. Figure 5b displays an SEM image of the carbon-deposited NP-TiO_2 IO (C-NP-TiO_2 IO) structure. NP-TiO_2 IO clearly displays a rough surface because of the presence of TiO_2 NPs compared to the high-C-TiO_2 IO sample (Figure 1d). We evaluated the surface area by indirectly quantifying the amount of dye adsorbed. Briefly, dye molecules that had been chemically adsorbed onto the TiO_2 surfaces were detached in a solution, and the concentration was quantified by comparison to a reference dye solution reported elsewhere;[42] the adsorption density was measured to be 0.0048 mmol cm^{-2} for high-C-TiO_2 IO and 0.0076 mmol cm^{-2} for high-C-NP-TiO_2 IO, respectively. Thus, the NP decoration enhanced the surface area by a factor of 1.8 relative to the corresponding undecorated surface. The photocatalytic activities of high-C-TiO_2 IO and high-C-NP-TiO_2 IO were compared. In Figure 5b, the initial rate of MB degradation of high-C-NP-TiO_2 IO was 0.406 min^{-1}, which was twice the value obtained in the presence of the high-C-TiO_2 IO structure (0.220 min^{-1}; Figure 4b). The enhancement ratio was comparable to the increase in the surface area.

Meanwhile, most photocatalytic degradation studies have examined water-based solution systems previously; however, many practical applications are complicated by the presence of a range of pollutant types and sizes (e.g., polymers, surfactants, particles), and solutions can be much more viscous than water solutions. In this case, mass transport of a pollutant into the porous photocatalyst rather determines the rate of the degradation reaction. Because it has been reported that the external flow penetrated the porous medium very little, even for the structure with a high void fraction,[43] the internal diffusion may determine the degradation rate. The effective diffusion coefficient for transport through the pores is proportional to the bulk diffusion coefficient and pore geometry; the bulk diffusion coefficient is inversely proportional to the solution viscosity, and the pore geometry is defined as φ/τ, where φ is the void fraction and τ is the pore tortuosity.[44] This implies that IO structures having macropores with high void fraction and low-tortuosity structures are expected to maintain a high photocatalytic activity in viscous solutions.[45]

The effects of the macroporous structure on the photocatalytic reaction were evaluated by comparing the C-TiO_2 IO structure with a mesoporous structure. A mesoporous film was fabricated by coating TiO_2 NP dispersion onto a substrate. The random packing of TiO_2 NPs formed mesopores with pore size of around 15 nm. φ of the TiO_2 NP film was in the range of 50−60%.[46] A viscous solution was prepared by dissolving 0.5 or 1 wt % PAA in the MB-containing water solution. The viscosity was measured to be around 0.05 Pa s for the 0.5 wt % PAA solution or around 0.4 Pa s for the 1.0 wt % PAA solution, respectively. Figure 6 shows that the degradation of MB

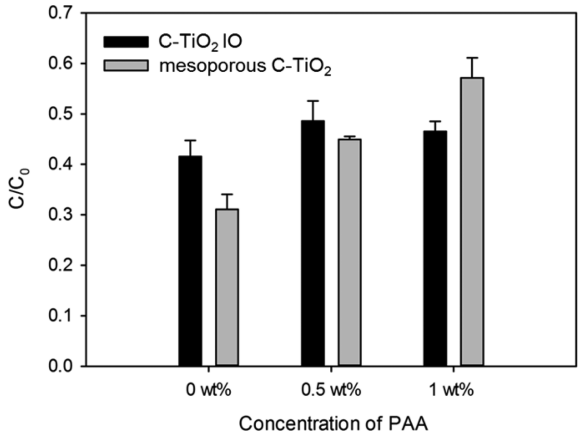

Figure 6. MB decomposition in the presence of the C-TiO_2 IO and mesoporous TiO_2 structures in a PAA solution.

measured 60 min after visible-light illumination. The film area of IO and mesoporous samples was controlled to possess a similar pore surface area. As the viscosity of the MB solution increased, both the macroporous C-TiO_2 IO and mesoporous C-TiO_2 films displayed a decrease in MB degradation, as expected; however, MB degradation of the C-TiO_2 IO film was relatively independent of the viscosity of the solution. By contrast, the mesoporous C-TiO_2 film displayed a greater loss in photocatalytic activity at higher solution viscosities. These results suggested that the effective diffusion coefficient of the IO structure is larger than that of the mesoporous film because of the pore morphology, resulting in relatively enhanced photocatalytic activity in a viscous solution.

CONCLUSIONS

We demonstrated the fabrication of C-TiO_2 IO structures and their application to visible-light photocatalysis. Carbon was deposited via high-temperature pyrolysis of a PF resol coating on the TiO_2 IO structure surface. The deposition formed an amorphous carbon layer on the TiO_2 surface and doped the carbon in the form of carbonate bonding into the TiO_2 interface. The carbon doping and carbon layer deposition on the TiO_2 surface shifted the band-gap edge into the visible region and enhanced visible-light absorption. The C-TiO_2 IO structure was evaluated as a visible-light photocatalyst. The photogenerated current under visible-light illumination was directly measured using solar cells constructed using the C-TiO_2 IO electrodes. The degradation of a model pollutant molecule, MB, was evaluated. Under visible-light illumination, only the high-C-TiO_2 IO structure displayed efficient photocatalytic activity. This activity was significantly enhanced by the greater capacity for visible-light absorption as a result of synergy between the carbon-sensitization and carbon-doping effects. A facile approach to enhancing the surface areas of C-TiO_2 IO structures was also introduced. The coating of TiO_2 NP increased the surface area by a factor of 2, further increasing the degradation rate accordingly. The activities of the C-TIO_2 IO structure under practical environmental conditions were tested by the photocatalytic performance in the presence of polymeric solutions having a range of viscosities. As the solution viscosity increased, the C-TiO_2 IO sample displayed a greater photocatalytic performance than only the mesoporous C-TiO_2 sample. These results were attributed to the larger pore size and lower-tortuosity pore in the C-TiO_2 IO structure.

ASSOCIATED CONTENT

Supporting Information

SEM images of PS colloidal crystals, Raman spectra of carbon-deposited samples, and Kulbelka–Munk transformed spectra. This material is available free of charge via the Internet at http://pubs.acs.org.

AUTHOR INFORMATION

Corresponding Author

*E-mail: junhyuk@sogang.ac.kr.

Author Contributions

‡These authors equally contributed to this work.

Notes

The authors declare no competing financial interest.

ACKNOWLEDGMENTS

This work was supported by grants from the National Research Foundation of Korea (Grant 2011-0030250) and the Sogang University Research Grant (SRF-201314004). The Korea Basic Science Institute is also acknowledged for the SEM and XPS measurements.

REFERENCES

(1) Pramauro, E.; Vincenti, M.; Augugliaro, V.; Palmisano, L. *Environ. Sci. Technol.* **1993**, *27*, 1790–1795.
(2) Zhang, Y. H.; Tang, Z. R.; Fu, X. Z.; Xu, Y. J. *ACS Nano* **2010**, *4*, 7303–7314.
(3) Oregan, B.; Gratzel, M. *Nature* **1991**, *353*, 737–740.
(4) Wang, Z. R.; Wang, H.; Liu, B.; Qiu, W. Z.; Zhang, J.; Ran, S. H.; Huang, H. T.; Xu, J.; Han, H. W.; Chen, D.; Shen, G. Z. *ACS Nano* **2011**, *5*, 8412–8419.
(5) Khan, S. U. M.; Al-Shahry, M.; Ingler, W. B. *Science* **2002**, *297*, 2243–2245.
(6) Hartmann, P.; Lee, D. K.; Smarsly, B. M.; Janek, J. *ACS Nano* **2010**, *4*, 3147–3154.
(7) Chen, H. H.; Nanayakkara, C. E.; Grassian, V. H. *Chem. Rev.* **2012**, *112*, 5919–5948.
(8) Linsebigler, A. L.; Lu, G. Q.; Yates, J. T. *Chem. Rev.* **1995**, *95*, 735–758.
(9) Lin, C. J.; Liou, Y. H.; Zhang, Y. C.; Chen, C. L.; Dong, C. L.; Chen, S. Y.; Stucky, G. D. *Appl. Catal., B* **2012**, *127*, 175–181.
(10) Wang, J.; Mao, B.; Gole, J. L.; Burda, C. *Nanoscale* **2010**, *2*, 2257–2261.
(11) In, S.; Orlov, A.; Berg, R.; Garcia, F.; Pedrosa-Jimenez, S.; Tikhov, M. S.; Wright, D. S.; Lambert, R. M. *J. Am. Chem. Soc.* **2007**, *129*, 13790–13791.
(12) Sakthivel, S.; Kisch, H. *Angew. Chem., Int. Ed.* **2003**, *42*, 4908–4911.
(13) Nguyen, T.-V.; Wu, J. C. S.; Chiou, C.-H. *Catal. Commun.* **2008**, *9*, 2073–2076.
(14) Bae, E.; Choi, W. *Environ. Sci. Technol.* **2003**, *37*, 147–152.
(15) Li, G.-S.; Zhang, D.-Q.; Yu, J. C. *Environ. Sci. Technol.* **2009**, *43*, 7079–7085.
(16) Chen, C.; Cai, W.; Long, M.; Zhou, B.; Wu, Y.; Wu, D.; Feng, Y. *ACS Nano* **2010**, *4*, 6425–6432.
(17) Zhong, J.; Chen, F.; Zhang, J. *J. Phys. Chem. C* **2010**, *114*, 933–939.
(18) Gu, D.-e.; Lu, Y.; Yang, B.-c.; Hu, Y.-d. *Chem. Commun.* **2008**, 2453–2455.
(19) Irie, H.; Watanabe, Y.; Hashimoto, K. *Chem. Lett.* **2003**, *32*, 772–773.
(20) Li, Y. Z.; Hwang, D. S.; Lee, N. H.; Kim, S. J. *Chem. Phys. Lett.* **2005**, *404*, 25–29.
(21) Park, Y.; Kim, W.; Park, H.; Tachikawa, T.; Majima, T.; Choi, W. *Appl. Catal., B* **2009**, *91*, 355–361.
(22) Lee, W. J.; Lee, J. M.; Kochuveedu, S. T.; Han, T. H.; Jeong, H. Y.; Park, M.; Yun, J. M.; Kwon, J.; No, K.; Kim, D. H.; Kim, S. O. *ACS Nano* **2012**, *6*, 935–943.
(23) Kochuveedu, S. T.; Jang, Y. J.; Jang, Y. H.; Lee, W. J.; Cha, M. A.; Shin, H.; Yoon, S.; Lee, S. S.; Kim, S. O.; Shin, K.; Steinhart, M.; Kim, D. H. *Green Chem.* **2011**, *13*, 3397–3405.
(24) Du, J.; Lai, X. Y.; Yang, N. L.; Zhai, J.; Kisailus, D.; Su, F. B.; Wang, D.; Jiang, L. *ACS Nano* **2011**, *5*, 590–596.
(25) Kubacka, A.; Fernandez-Garcia, M.; Colon, G. *Chem. Rev.* **2012**, *112*, 1555–1614.
(26) Paramasivam, I.; Jha, H.; Liu, N.; Schmuki, P. *Small* **2012**, *8*, 3073–3103.
(27) Choi, S. K.; Kim, S.; Lim, S. K.; Park, H. *J. Phys. Chem. C* **2010**, *114*, 16475–16480.
(28) Cesano, F.; Bertarione, S.; Damin, A.; Agostini, G.; Usseglio, S.; Vitillo, J. G.; Lamberti, C.; Spoto, G.; Scarano, D.; Zecchina, A. *Adv. Mater.* **2008**, *20*, 3342–3348.
(29) Liu, S. Q.; Zhang, N.; Tang, Z. R.; Xu, Y. J. *ACS Appl. Mater. Interfaces* **2012**, *4*, 6378–6385.
(30) Li, G. S.; Zhang, D. Q.; Yu, J. C. *Environ. Sci. Technol.* **2009**, *43*, 7079–7085.
(31) Wang, X. C.; Yu, J. C.; Hou, Y. D.; Fu, X. Z. *Adv. Mater.* **2005**, *17*, 99–102.
(32) Li, Y. Z.; Kunitake, T.; Fujikawa, S. *J. Phys. Chem. B* **2006**, *110*, 13000–13004.
(33) Chen, H. A.; Chen, S.; Quan, X.; Zhang, Y. B. *Environ. Sci. Technol.* **2010**, *44*, 451–455.
(34) Chen, J. I. L.; von Freymann, G.; Kitaev, V.; Ozin, G. A. *J. Am. Chem. Soc.* **2007**, *129*, 1196–1202.
(35) Kim, J. K.; Moon, J. H.; Lee, T. W.; Park, J. H. *Chem. Commun.* **2012**, *48*, 11939–11941.
(36) Sun, S. M.; Wang, W. Z.; Zhang, L.; Xu, J. H. *Appl. Catal., B* **2012**, *125*, 144–148.
(37) Hagfeldt, A.; Boschloo, G.; Sun, L. C.; Kloo, L.; Pettersson, H. *Chem. Rev.* **2010**, *110*, 6595–6663.

(38) Zhang, J.; Li, M. J.; Feng, Z. C.; Chen, J.; Li, C. *J. Phys. Chem. B* **2006**, *110*, 927−935.
(39) Zhang, P.; Shao, C.; Zhang, Z.; Zhang, M.; Mu, J.; Guo, Z.; Liu, Y. *Nanoscale* **2011**, *3*, 2943−2949.
(40) Ren, W.; Ai, Z.; Jia, F.; Zhang, L.; Fan, X.; Zou, Z. *Appl. Catal., B* **2007**, *69*, 138−144.
(41) Wu, G.; Nishikawa, T.; Ohtani, B.; Chen, A. *Chem. Mater.* **2007**, *19*, 4530−4537.
(42) Kim, H. N.; Yoo, H.; Moon, J. H. *Nanoscale* **2013**, *5*, 4200−4204.
(43) James, D. F.; Davis, A. M. J. *J. Fluid Mech.* **2001**, *426*, 47−72.
(44) Davis, M. E. Davis, R. J. *Fundamentals of Chemical Reaction Engineering*, 1st ed.; McGraw-Hill: New York, 2002.
(45) Umeda, G. A.; Chueh, W. C.; Noailles, L.; Haile, S. M.; Dunn, B. S. *Energy Environ. Sci.* **2008**, *1*, 484−486.
(46) Benkstein, K. D.; Kopidakis, N.; van de Lagemaat, J.; Frank, A. J. *J. Phys. Chem. C* **2003**, *107*, 7759−7767.